



**HAL**  
open science

# Representative elementary volume assessment of three-dimensional x-ray microtomography images of heterogeneous materials: Application to limestones

Olivier Rozenbaum, Sabine Rolland Du Roscoat

► **To cite this version:**

Olivier Rozenbaum, Sabine Rolland Du Roscoat. Representative elementary volume assessment of three-dimensional x-ray microtomography images of heterogeneous materials: Application to limestones. *Physical Review E: Statistical, Nonlinear, and Soft Matter Physics*, 2014, 89 (053304), 11 p. 10.1103/PhysRevE.89.053304 . insu-00991067

**HAL Id: insu-00991067**

**<https://insu.hal.science/insu-00991067>**

Submitted on 14 May 2014

**HAL** is a multi-disciplinary open access archive for the deposit and dissemination of scientific research documents, whether they are published or not. The documents may come from teaching and research institutions in France or abroad, or from public or private research centers.

L'archive ouverte pluridisciplinaire **HAL**, est destinée au dépôt et à la diffusion de documents scientifiques de niveau recherche, publiés ou non, émanant des établissements d'enseignement et de recherche français ou étrangers, des laboratoires publics ou privés.

# Representative elementary volume assessment of three-dimensional x-ray microtomography images of heterogeneous materials: Application to limestones

O. Rozenbaum<sup>1,\*</sup> and S. Rolland du Roscoat<sup>2,†</sup><sup>1</sup>*Institut des Sciences de la Terre d'Orléans (ISTO), UMR 7327–CNRS/Université d'Orléans, 45071 Orléans; BRGM, BP36009 45060, France*<sup>2</sup>*Université Grenoble Alpes, 3SR Lab, CNRS, 38041 Grenoble Cedex 9, France*

(Received 9 December 2013; published 13 May 2014)

Over the last 15 years, x-ray microtomography has become a useful technique to obtain morphological, structural, and topological information on materials. Moreover, these three-dimensional (3D) images can be used as input data to assess certain properties (e.g., permeability) or to simulate phenomena (e.g., transfer properties). In order to capture all the features of interest, high spatial resolution is required. This involves imaging small samples, raising the question of the representativity of the data sets. In this article, we (i) present a methodology to analyze the microstructural properties of complex porous media from 3D images, (ii) assess statistical representative elementary volumes (REVs) for such materials; and (iii) establish criteria to delimit these REVs. In the context of cultural heritage conservation, a statistical study was done on 30 quarry samples for three sorts of stones. We first present the principles of x-ray microtomography experiments and emphasize the care that must be taken in the 3D image segmentation steps. Results show that statistical REVs exist for these media and are reached for the image sizes studied ( $1300 \times 1300 \times 1000$  voxels) for two characteristics: porosity and chord length distributions. Furthermore, the estimators used (porosity, autocorrelation function, and chord length distributions) are sufficiently sensitive to quantitatively distinguish these three porous media from each other. Lastly, this study puts forward criteria based on the above-mentioned estimators to evaluate the REVs. These criteria avoid having to repeat the statistical study for each new material studied. This is particularly relevant to quantitatively monitor the modifications in materials (weathering, deformation . . .) or to determine the smallest 3D volume for simulation in order to reduce computing time.

DOI: [10.1103/PhysRevE.89.053304](https://doi.org/10.1103/PhysRevE.89.053304)

PACS number(s): 07.05.Pj, 81.05.Rm, 81.70.Tx

## I. INTRODUCTION

Natural materials such as bones, snow, stones, or sand, and manmade materials such as paper, fluidized beds, or concrete, are examples of porous media. These materials are studied in order to characterize their microstructural properties, to better understand and/or better predict their behavior, and to improve their end-use properties in the case of manmade materials. Such analyses require a thorough three-dimensional (3D) description of the microstructure. For example, in the case of building stone conservation, analyses focus on deterioration properties and especially on weathering effects. Weathering is governed mainly by water transfer within the stones and is highly dependent on the structural characteristics, i.e., morphology, texture, and topology. A prerequisite for modeling weathering mechanisms is to characterize weathered stones from buildings and unweathered stones extracted from quarries or from buildings, but in places where the sampled stones can be assumed to be unweathered by environmental agents. Simulations and models to predict weathering require a realistic tridimensional description of the phases constituting the materials.

A powerful “nondestructive” method to characterize the 3D inner microstructure of porous materials at the micrometer scale is x-ray computed tomography (XCT). First developed for materials science in synchrotron facilities, this technique is now widely used for the 3D characterization of materials [1–6] due to laboratory setups that are fully competitive.

Thanks to continuous improvements in x-ray tubes and x-ray detectors, laboratory systems can now achieve resolutions down to  $1 \mu\text{m}$ . Investigating a given characteristic or property on realistic 3D images entails capturing all the features at the scale of interest of the phenomenon, i.e., the pore scale in the case of porous media. In most cases, therefore, high spatial resolution is required, which means imaging small samples.

However, working with small samples raises the question of the representativity of the data sets: are the microstructural characteristics or physical properties determined on the 3D volumes representative of the macroscopic characteristics or properties? Furthermore, in some cases where simulations are time consuming, it is interesting to investigate the properties on the smallest possible volume. Different definitions of a representative elementary volume (REV) can be found in the literature (e.g., [7,8]).

Despite the fact that these definitions result in different strategies to assess properties and in different REV sizes, they all respect the separation scale  $l_{\text{micro}} \ll l_{\text{REV}} \ll l_{\text{macro}}$ , where  $l_{\text{micro}}$ ,  $l_{\text{REV}}$ , and  $l_{\text{macro}}$  denote, respectively, the characteristic length at the microscale, the representativity, and the macroscale. The separation scale means that the volume is small enough to capture the microstructural features and large enough to represent the macroscopic property. The REV is much larger than heterogeneities such as grains or pores but should be smaller than the macroscopic structural dimensions. The second common point of these definitions is the fact that the REV is estimated for a given characteristic or property [9,10] and must be independent of the point of calculation (localization of the volume in 3D space). Al-Raoush and Papadopoulos [10] showed, for example, that

\*rozenbaum@cnsr-orleans.fr

†sabine.rollandduroscoat@3sr-grenoble.fr

the REV determined for porosity is smaller than the REV determined for particle size or coordination number. However, these approaches present the drawback of being difficult to implement or are biased.

Nevertheless, many procedures have been proposed in the literature to determine the representative volume [7,11–15]. One possibility is to evaluate the “deterministic” REV [7,8,16,17], which is implemented by taking a small volume within an image and calculating the property of interest (e.g., porosity). The small volume is then expanded in all directions and the property is recalculated. The “deterministic” REV is then determined as the volume value over which the property of interest remains constant [7].

Another approach is using the “statistical” REV [16,18–20], defined as the size of a volume beyond which the mean of the estimated property (or characteristic) becomes approximately constant, and the coefficient of variation, defined as the ratio between the standard deviation and the mean, is less than a given value. Hence, a given characteristic in a heterogeneous material can be determined either by a few measurements on large volumes, or by measurements of many small volumes of material. The key point in this approach is that the “statistical” REV must be considered as a function of several parameters, including the physical property, the contrast of properties, the volume fractions of components, the desired relative precision for the estimation of the property, and the number of independent samples at one’s disposal.

In the literature dealing with quantitative 3D image analysis obtained from XCT measurement, it is often assumed that the REV exists and is smaller than the maximum imaged volume. However, this hypothesis is not always verified (and is rarely the case in building stone conservation studies). The aim of the present article is therefore to propose a methodology to analyze the microstructural properties of stones used in historical buildings, and beyond that, a methodology that can be extended to all such complex materials. This method is illustrated using three different stones described in Sec. II A: (i) the samples were imaged using microtomography (Sec. II B), (ii) the data sets obtained were preprocessed (Sec. II C) before (iii) microstructural measurements of porosity, autocorrelation length and chord distribution (Sec. II D), and the representativity of the data sets was then analyzed (Sec. II E). Results are presented and discussed in Sec. III, where we focus in particular on the existence of REV, and the possibility of distinguishing these stones by image analysis. Section IV summarizes our conclusions.

## II. MATERIALS AND METHODS

### A. Stones

The Saint-Maximin limestones analyzed in this study come from a quarry to the north of Paris (Saint-Maximin, France). Two sediment beddings commercially denoted “Roche Franche” (RF) and “Roche Franche Fine” (RFF) were selected. These stones were widely used in the construction of monuments in Paris [21]. These rocks, formed 45 million years ago, are beige-colored sedimentary limestones composed essentially of calcite and quartz. Although they appear globally similar to the naked eye, the RF bedding is coarse grained while

the RFF stone has finer solid phases but with large fossils. Their porosities, determined by hydrostatic weighing [22], are about 0.35 (RF) and 0.25 (RFF). The samples used in this study were rod samples drilled parallel to the stone bed. Two blocks of RF stones from two quarries (denoted hereafter RF1 and RF2) and a single one for RFF were selected. For the three different types of stone (RF1, RF2, and RFF), ten cylinders, 6 mm in diameter, were drilled. Note that each set of ten samples was extracted from a small volume (less than 10 cm<sup>3</sup>) in order to preserve local properties.

### B. X-ray microtomography

For 3D image acquisition by x-ray microtomography, a specimen is placed on a rotary stage between the x-ray source and the detector. The specimen is rotated step by step, taking one projection image at each angular position. Due to absorption by the material, the x-ray beam is attenuated when passing through a specimen. The change in intensity of the x-ray beam is recorded, resulting in gray level images (projections). Using a filtered back projection algorithm, a computer reconstructs the projections to obtain cross-sectional images of the sample (tomograms). Stacking these reconstructed images forms a 3D image of the sample (volume dataset). At each space position of the resulting dataset, a gray value corresponds to the effective x-ray attenuation coefficient. Hence, if the principal compounds of the object are known and have a sufficient density contrast, the distribution of these compounds within the object can be easily deduced. Theoretically, with a monochromatic x ray (e.g., from a synchrotron beamline), the relation between pixel value (attenuation coefficient) and the compound’s mass density is well defined by the Beer-Lambert equation [23]. With a polychromatic x-ray beam, which is the case for laboratory XCT, artifacts are inevitable and difficult to remove.

It is therefore difficult to associate pixel values with material densities in an absolute and quantitative manner. Frequently encountered artifacts include: (i) the beam hardening effect [24], where an object of uniform density appears to have a thick and dense skin, or (ii) the ring effect [25], generally caused by temporary and spurious bad pixels in the detector. These effects can be reduced by the reconstruction software, but only to a certain extent and less effectively for a multicomponent object. For the stone samples, microtomography analyses were performed using an industrial XCT device Nanotom 180NF (GE Phoenix|x-ray, Wunstorf, Germany) available at the ISTO. This unit has a 180-kV nanofocus x-ray tube and a digital detector array (2304 × 1152 pixels, Hamamatsu detector). Samples were placed in the chamber and rotated by 360 deg during acquisition. The resulting projections were converted into a 3D image stack using a microcluster of four personal computers (PCs) with the Phoenix 3D reconstruction software (filtered backprojection Feldkamp algorithm [26]). The reconstruction software contains several different modules for artifact reduction (beam hardening, ring artifacts) to optimize the results. Finally, the 16-bit 3D image is converted into an 8-bit image (256 gray levels) before preprocessing. The samples were mounted and waxed on a glass rod. An operating voltage of 110 kV and a filament current of 59  $\mu$ A were applied. The distance between the x-ray source and the sample

and between the x-ray source and the detector was 15 and 500 mm, respectively, giving a voxel size of  $3 \mu\text{m}$ . The 2000 projection images (angular increment of  $0.18^\circ$ ) were acquired during stone rotation (with an acquisition time of 4 hours). As the cone beam geometry created artifacts, the first and the last 76 cross-sectional images were removed. The volume of interest that was selected was a cube of  $1300 \times 1300 \times 1000$  voxels (1000 cross-sectional images) representing a volume of  $3.9 \times 3.9 \times 3.0 \text{ mm}^3$ .

**C. Preprocessing**

One of the main objectives of 3D image analysis is to retrieve reliable quantitative measures of the features of interest. Prior to estimating characteristics (e.g., porosity, specific surface, Euler number) or simulating properties (e.g., conductivity, permeability) on these 3D images, the different phases have to be distinguished (segmentation step), since image quantification requires proper segmentation of the solid and void phases. Segmentation is the process of partitioning the gray level voxels of the 3D image into distinct phases. Unfortunately, artifacts and/or noise often prevent segmentation of these 3D images [27]: acquired real data are usually noisy, with a signal-to-noise ratio depending on the quality of the acquisition equipment. If the data are acquired from a laboratory-CT scanner, the noise may be linked to blurring, partial volume effect, hardening of the beam, or due to its conical geometry, making the reconstruction difficult.

Hence, in addition to acquiring high-quality images, one must preprocess the images in order to minimize these drawbacks. This consists in a noise reduction (filtering), followed by a thresholding step. The preprocessing step was

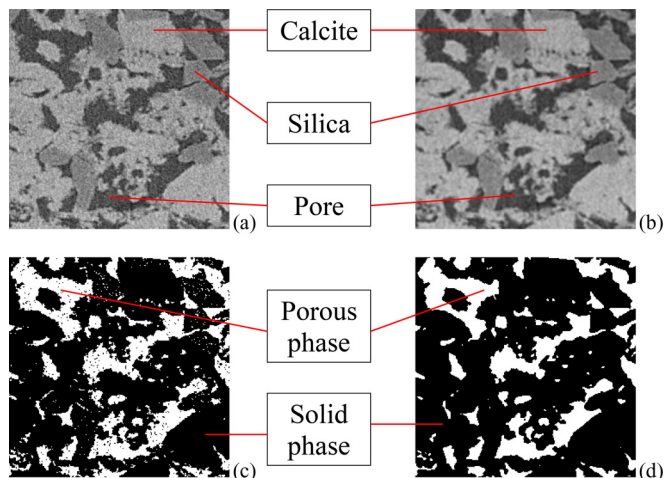


FIG. 1. (Color online) (a) 2D zoom of an original image from one of the ten RF1 samples ( $256 \times 256$  pixels). The dark gray levels correspond to the pore phase, medium gray levels to the silica phase, and light gray levels to the calcite phase. (b) Image (a) after application of the mean filter. (c) thresholding of image (a), where the pore phase is in white (the solid phase is in black). (d) thresholding of image (b), where the pore phase is in white (the solid phase is in black).

done by algorithms developed by Le Trong *et al.* [28], which are detailed below.

**1. Filtering**

As the gray level value of a voxel is related to the x-ray absorption of the sample at the voxel position, pores appear in dark gray, silica compounds in medium gray and calcite compounds in light gray [Fig. 1(a)]. Even if these different phases are distinguishable to the naked eye, direct thresholding of the original image is not possible. As previously explained, this is related to the presence of noise that restricts the selection of a gray level as the limit between the solid and void phases. Thus, the signal-to-noise ratio (SNR) of the original 3D image of one of the RF1 samples presented in Fig. 1(a) was 3.48. The SNR of an image is defined here as the ratio of its mean value to its standard deviation [29].

Figure 2 shows that the histogram of this 3D original image presents only two distributions. This indicates that the calcite and silica phases have a very large overlap in the histogram (within the [100, 255] gray level range) and are not separable with this histogram. In other words, some voxels with a given gray level can belong either to the calcite phase or to the silica phase. As shown in the following, this phenomenon is also encountered for voxel gray levels around 100, even if a minimum is present.

Hence, most of the segmentation complexity is related to the presence of noise and blur (the borders between the phases are not well defined) [28]. To solve this problem, different filters (mean and median filters and closing-opening) were applied for noise reduction [30]. The 3D mean filter with a kernel of  $3 \times 3 \times 3$  voxels [30] was found optimum to minimize the noise without (too much) loss of information (loss of smaller details only). After application of the mean filter, the SNR reached 3.90 [compare Figs. 1(a) and 1(b)]. The histogram of the filtered image contrasts strongly with that of the original image (Fig. 2), as three distributions were distinguishable.

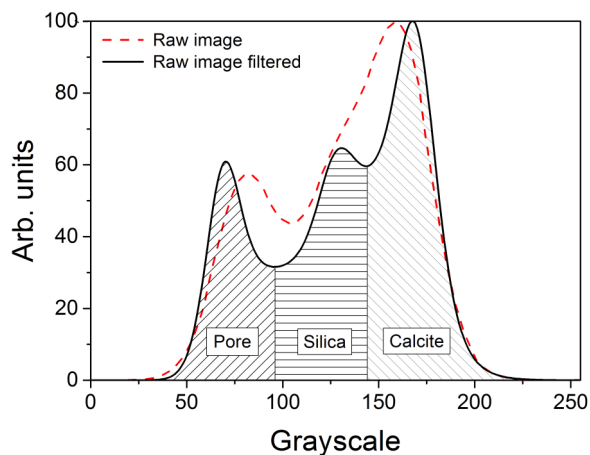


FIG. 2. (Color online) Gray scale histograms recorded for the original image and after the mean filter operation on the sample shown in Figs. 1(a) and 1(b). For the filtered original image, the [0–93] gray levels correspond to the pore phase, the [94–143] gray levels to the silica phase, and the [144–255] gray levels to the calcite phase.



## 2. Thresholding

The second step in image preprocessing is thresholding. As after the filtering step three distributions are easily distinguished (Fig. 2), direct thresholding of the phases is possible. The thresholds are the gray values corresponding to the local minima of the histogram. Hence, all the voxels belonging (i) to the  $[0, \xi_L]$  range represent the pore phase, (ii) to the  $[\xi_L, \xi_H]$  range represent the silica phase, and (iii) to the  $[\xi_H, 255]$  range represent the calcite phase. As the transfer of water in stones is the main focus of interest, the threshold value used here was  $\xi_L$  (for the ten RF1 and ten RF2 stone samples  $\xi_L \in [90, 99]$  and for the ten RFF stone samples levels  $\xi_L \in [77, 96]$ ). In other words, the value 1 was assigned to the porous phase (gray levels  $\in [0, \xi_L]$ ), and the value 0 to the solid phase (gray levels  $\in [\xi_L, 255]$ ). After segmentation, a binarized image was obtained and is represented by only two phases.

Hence for the 3D image presented as an example [Fig. 3(a)], an optimum thresholding value of  $\xi_L = 93$  was obtained for the 3D filtered image (Fig. 2). Figures 1(d) and 3(c) show the filtered image thresholded at the minimum between the first two distributions ( $\xi_L = 93$ ). Comparison of ten segmented

two-dimensional (2D) images located approximately regularly along the 3D image with their respective 256 gray level 2D images [see Figs. 1(b) and 1(d) and see Figs. 3(b) and 3(c)] showed that the segmentation could be considered as satisfactory (pore phase in white and solid phase in black with few errors).

Note that thresholding the original image at the minimum gray level between the two distributions [ $\xi_L = 104$  for the example in Fig. 1(a)], i.e., without the filtering step, led to a binarized image [Fig. 1(c)] with a lot of “bad” voxels (black voxels in a white phase and vice versa). As a result, the porosity of the segmented original image was 28.87%, while that of the filtered image was 24.72%. This indicates again that the porous and solid phases have a very large overlap in the histogram (some voxels with a given gray level can belong either to the porous phase or to the solid phase) and that the filtering step is obligatory (denoising step).

## D. Structural parameters

Different estimators were then calculated on the segmented images. Most of these estimators were described in Refs. [31–33].

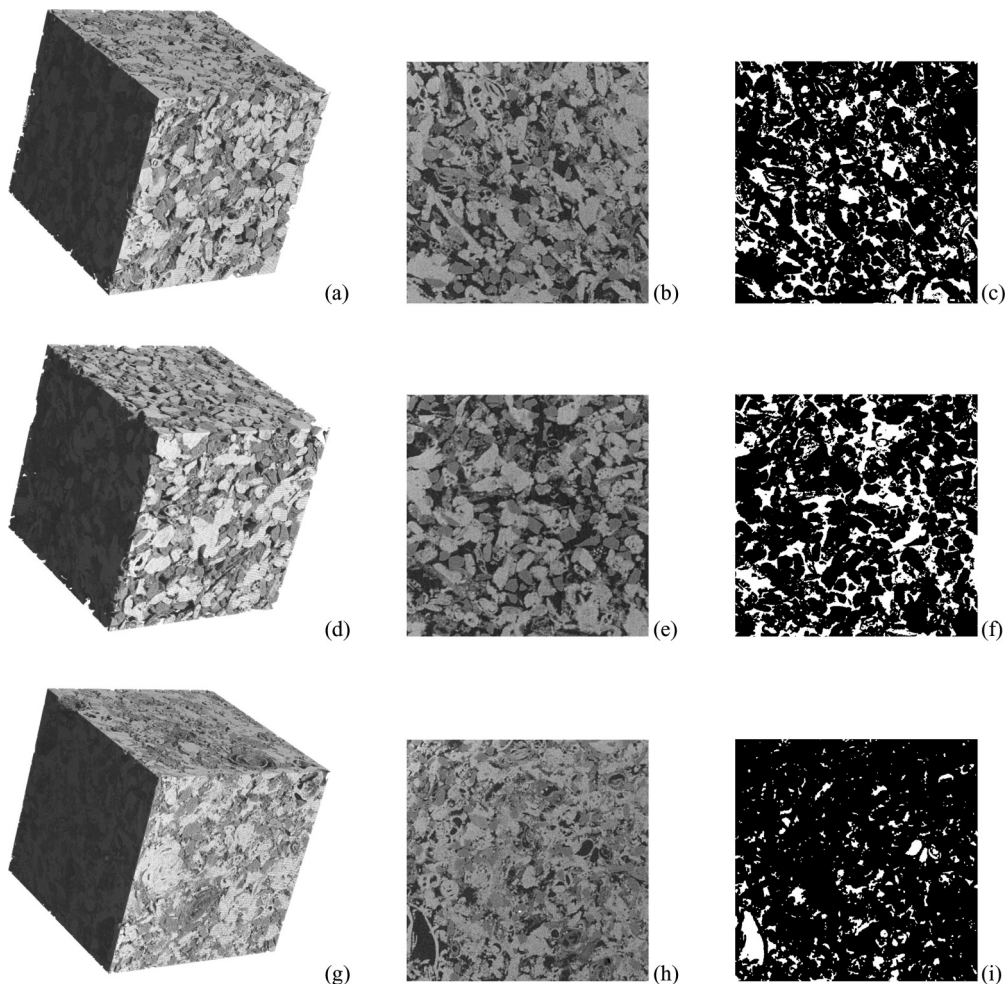


FIG. 3. 3D images of the RF1 (a), RF2 (d), and RFF stones (g) after the filtering step. The images were visualized by using VG-Studio software.<sup>1</sup> The volume dimensions are  $800 \times 800 \times 800$  voxels. The pore phase is transparent; the medium gray levels correspond to the silica phase, and light gray levels to the calcite phase. 2D cuts of the 3D volumes are represented in Figs. 3(b), 3(e), and 3(h) for the RF1, RF2, and RFF stones, respectively. Segmentations of these 2D cuts are reported in Figs. 3(c), 3(f), and 3(i).

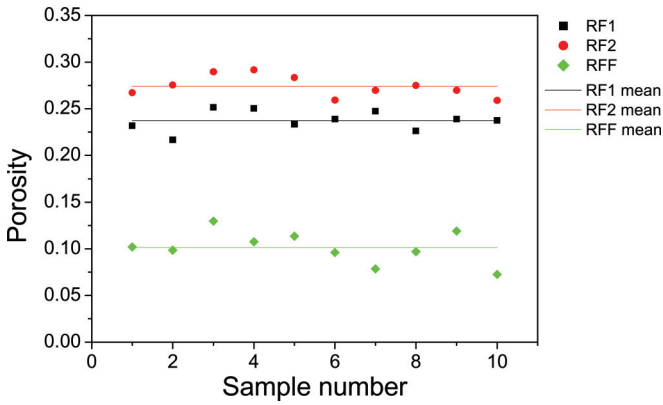


FIG. 4. (Color online) Characterization of the porosity for the 30 analyzed samples. The porosities were calculated on the whole sample volumes ( $1300 \times 1300 \times 1000$  voxels). The continuous lines are the mean values obtained from the ten values available for each sort of stone.

**1. Porosity**

Total porosity ( $\phi$ ) is defined as follows:

$$\phi = \frac{V_p}{V_p + V_s}, \tag{1}$$

$$L = \int_0^\infty R_Z(r) dr. \tag{2}$$

where  $V_p$  and  $V_s$  are the volume of the pore and solid phase, respectively. For a 3D digitized medium,  $V_p$  and  $V_s$  are the number of voxels corresponding, respectively, to the porous phase and to the solid phase.

**2. Autocorrelation function**

The autocorrelation function  $R_Z(\vec{r})$  is a statistical description of a porous medium [31,33]. This function can be interpreted as the probability of finding two randomly selected points that are both in the same phase at a given distance  $|r|$ . For an isotropic medium with  $r = |\vec{r}|$ ,  $R_Z(\vec{r}) = R_Z(r)$ , the autocorrelation function depends on distance alone. Otherwise, the one-dimensional autocorrelation functions for  $\vec{r}$  parallel to the  $Ox$ ,  $Oy$ , or  $Oz$  axis (where  $Ox$ ,  $Oy$ , and  $Oz$  define an orthogonal reference), respectively noted  $R_{Zx}$ ,  $R_{Zy}$ , and  $R_{Zz}$ , give information about isotropy or anisotropy, since pore space anisotropy is revealed as a disparity between the one-dimensional autocorrelation functions along different directions. A characteristic length scale is  $L$ , defined as the integral of the autocorrelation function. It represents a length scale characteristic of the spatial structure [34]:

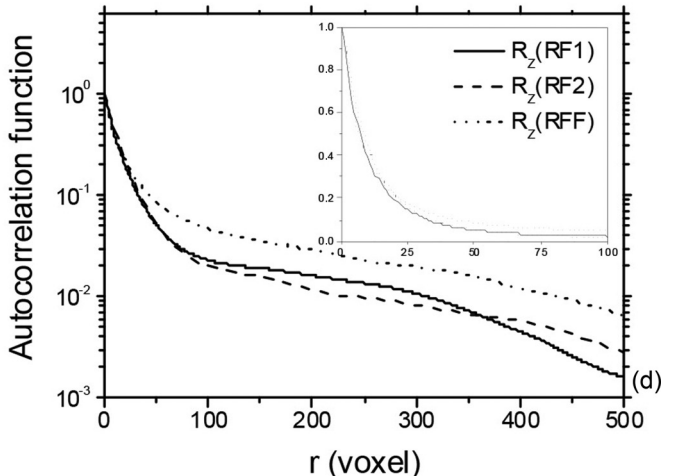
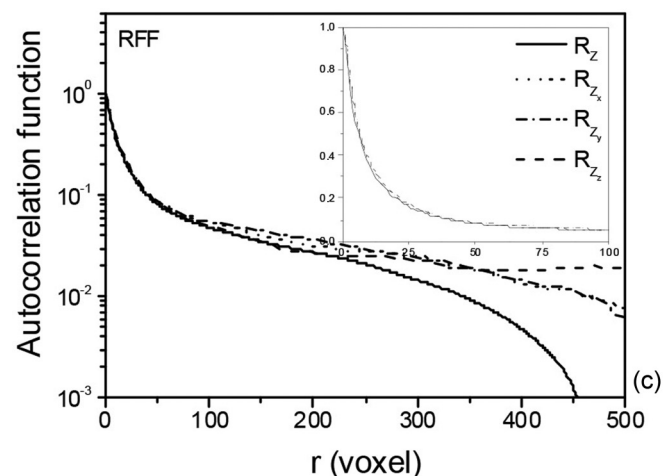
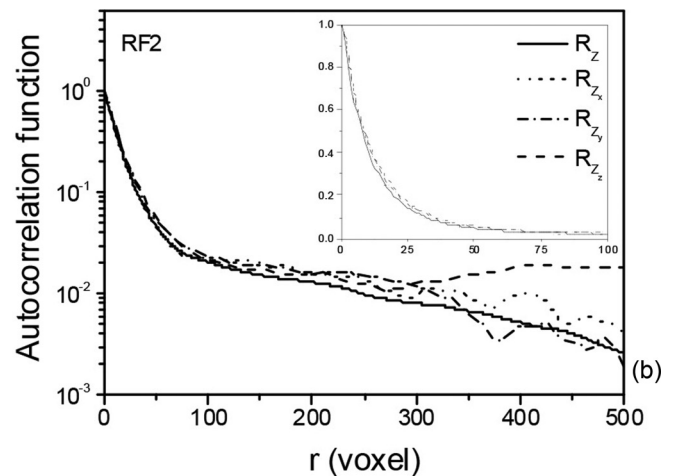
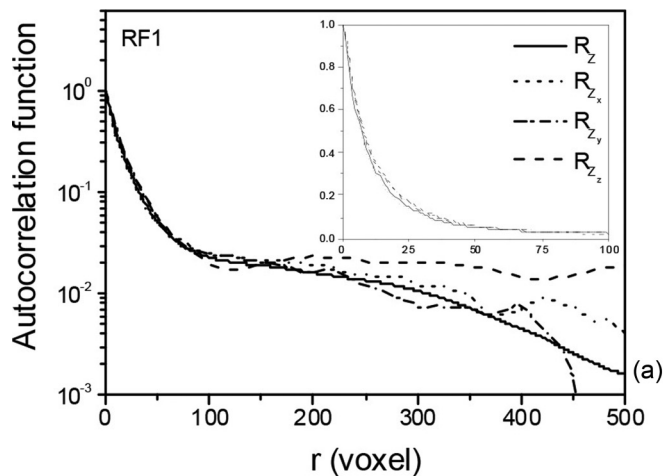


FIG. 5. Autocorrelation functions ( $R_{Zx}$ ,  $R_{Zy}$ , and  $R_{Zz}$ ) and the average value  $R_Z$  for a RF1 sample (a), a RF2 sample (b), and a RFF sample (c).

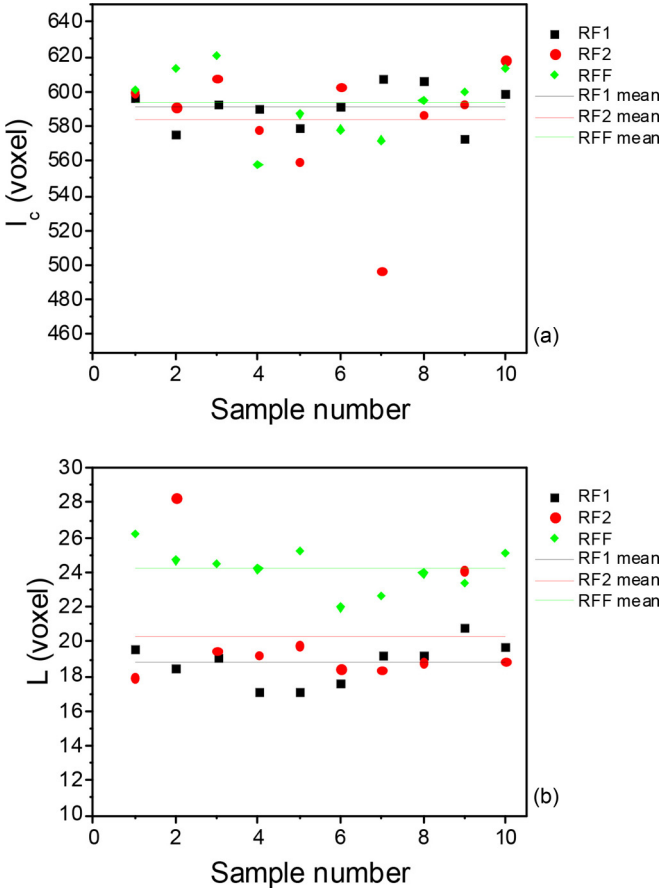


FIG. 6. (Color online) Characterization of the autocorrelation functions for the 30 analyzed samples. These characteristics were calculated on the whole sample volumes ( $1300 \times 1300 \times 1000$  voxels). Correlation lengths  $l_c$  (a) and integrals of the autocorrelation functions  $L$  (b). The continuous lines are the mean values of the ten values recorded for each sort of stone.

Another length scale obtainable from the autocorrelation function is its correlation length  $l_c$ , defined as the distance at which the autocorrelation function falls to zero. This parameter  $l_c$  provides a convenient length scale beyond which correlations have died out.  $l_c$  represents a length scale characterizing the short-range order due to exclusion-volume effects (impenetrable objects) and is significantly larger than the typical grain size [35].

### 3. Chord distribution

Chord distributions are stereological tools used to describe the interface between pore and solid phases [31,33]. The chord distribution gives the probability of having a chord length between  $r$  and  $r + dr$ . Chord distribution can be calculated either for the pores [ $f_p(r)$ , or pore chord distribution] or for the solid [ $f_s(r)$ , or solid chord distribution]. A particular case is distinguishable if both the pore and solid chord distributions present exponential decreases. This type of porous medium is called a long-range random medium [31,32]. In other words, the pore and solid phases in the datasets are randomly distributed. The mathematical expressions of these exponential

decrease distributions are [e.g., 32]

$$f_p(r) \equiv e^{(-r/\alpha_p)} \quad (3)$$

and

$$f_s(r) \equiv e^{(-r/\alpha_s)}, \quad (4)$$

where  $\alpha_p$  is the persistence length for the porous phase and  $\alpha_s$  is the persistence length for the solid phase.

### E. REV estimation

In this work, we decided to analyze the representativity of our data sets using two of the statistical approaches found in the literature [18–20]. Both approaches specify that the REV size depends on the property studied and on the acceptable accuracy to estimate it, as well as on the number of independent realizations that can be measured. The main difference between these two approaches lies in the definition of the accuracy of the result.

Gusev [20] investigated the properties for  $n$  independent subvolumes of different sizes. He defined the REV volume thus: the average made of the estimation “should be accurate enough and the scatter of the estimates should be small.” The scatter was defined as  $\frac{D_p^2(V)}{\sqrt{n}}$ , where  $n$  is the number of realizations for each subvolume and  $D_p^2(V)$  is the variance obtained from the measurements of the properties  $P$  obtained on  $n$  subvolumes of size  $V$ .

Kanit *et al.* [18,19] refined this approach. The REV was defined as a function of the physical properties of each constituent, their contrast, the microstructure, the required precision, and the number of realizations. The size of this static REV  $V_{\text{REV}}$  depends on [18].

(1) The integral range  $A_3$  [36] that gives “information on the volume size of the structure for which the parameter measured in this volume has a convenient statistical representativity

- (2) The point variance of the considered property  $P, D_P$
- (3) The mean property  $P$
- (4) A relative error  $\varepsilon$
- (5) The number of realizations  $n$

via the following relationship in the case of structural properties such as porosity or persistence lengths:

$$V_{\text{REV}} = 4D_P^2 \frac{A_3}{n\varepsilon^2}. \quad (5)$$

The volume of the REV can be deduced from Eq. (5), and in the case of a cubic sample, an REV size that equals  $l_{\text{REV}} = V_{\text{REV}}^{1/3}$  can be defined.

The magnitude  $D_P^2 A_3$  can be experimentally obtained [16] from the following equation:

$$D_P^2(V) = D_P^2 \frac{A_3}{V}, \quad (6)$$

where  $D_P^2(V)$  is the variance obtained from the measurements of the properties  $P$  carried out on independent subvolumes of size  $V$ .

**III. RESULTS AND DISCUSSION**

**A. Data acquisition and preprocessing**

The 30 samples were measured and preprocessed (filtered and segmented) following the procedure described in Secs. II B and II C. Figure 3 illustrates the binarization steps for a single sample of each stone. 3D images were visualized by using VG-Studio software.<sup>1</sup> They correspond to cubes of  $800 \times 800 \times 800$  voxels. The differences in terms of porosity or pore sizes between the three types of stone can be observed on the 3D views, as well as on the 2D slices. At the observation scale, RFF clearly exhibits a smaller total porosity than both RF1 and RF2 stones. RF1 and RF2 stones look similar, while the RFF stone is less homogeneous with finer grains and pores. The presence of a large fossil [Figs. 3(h) and 3(i), on the left bottom corner] creates a large pore within this sample. This phenomenon is encountered throughout the volume.

**B. Structural parameters**

The measurements of the microstructural characteristics of the 30 samples are reported in Figs. 4–8 for porosities, correlation functions (and their characteristics), and chord distributions (and their characteristics), respectively. Table I gives the average values for each characteristic and the associated standard deviation.

**1. Porosity**

The pore volume fraction of the 30 stones was determined. Results are reported in Fig. 4 and Table I. For the three stone

types, the mean porosities obtained on the microtomographic data sets are smaller than those obtained by hydrostatic weighing. This comes from the fact that the experimental conditions chosen do not allow one to see details smaller than  $3^3 \mu\text{m}^3$  (voxel size) and pores smaller than this value account for a significant proportion of the porosity. A comparative study of the samples was therefore carried out at the observation scale, but it must be remembered that it only applies to pore sizes larger than  $3^3 \mu\text{m}^3$ . From the total porosities (Table I and Fig. 4), the RFF and RF1/RF2 types can be distinguished, as can the RF1 and RF2 stones. Hence, with porosity measurements alone, it is possible to distinguish the two sediment beddings of the RF1 and RF2 samples.

**2. Autocorrelation function**

The autocorrelation functions  $R_{Zx}$ ,  $R_{Zy}$ , and  $R_{Zz}$  and the average value  $R_Z$  for the 30 stones were determined. Examples of the results obtained for one stone from each series are shown in Figs. 5(a), 5(b), and 5(c) for a single RF1, RF2, and RFF sample, respectively. Similar results were obtained for all the samples belonging to the same stone. Except for the  $R_{Zz}$  function and for the large lags, no particular disparity was observed for the one-dimensional autocorrelation functions along the orthogonal directions ( $R_{Zx}$ ,  $R_{Zy}$ ) and  $R_Z$ . This means that these samples do not show any anisotropy in the bedding plane and present very slight anisotropy in the direction perpendicular to the sediment bedding. The absence of correlation peaks indicates that the analyzed stones are random media. Moreover,  $l_c$  and  $L$  were calculated from  $R_Z$  for the 30 samples (Fig. 6). Table I summarizes the mean  $l_c$  and  $L$  found for each type of rock. In the case of  $l_c$  values, no difference from the mean values was observed for any type of stone. This means that the autocorrelation function does not

<sup>1</sup>VG-Studio software, <http://www.volumegraphics.com>.

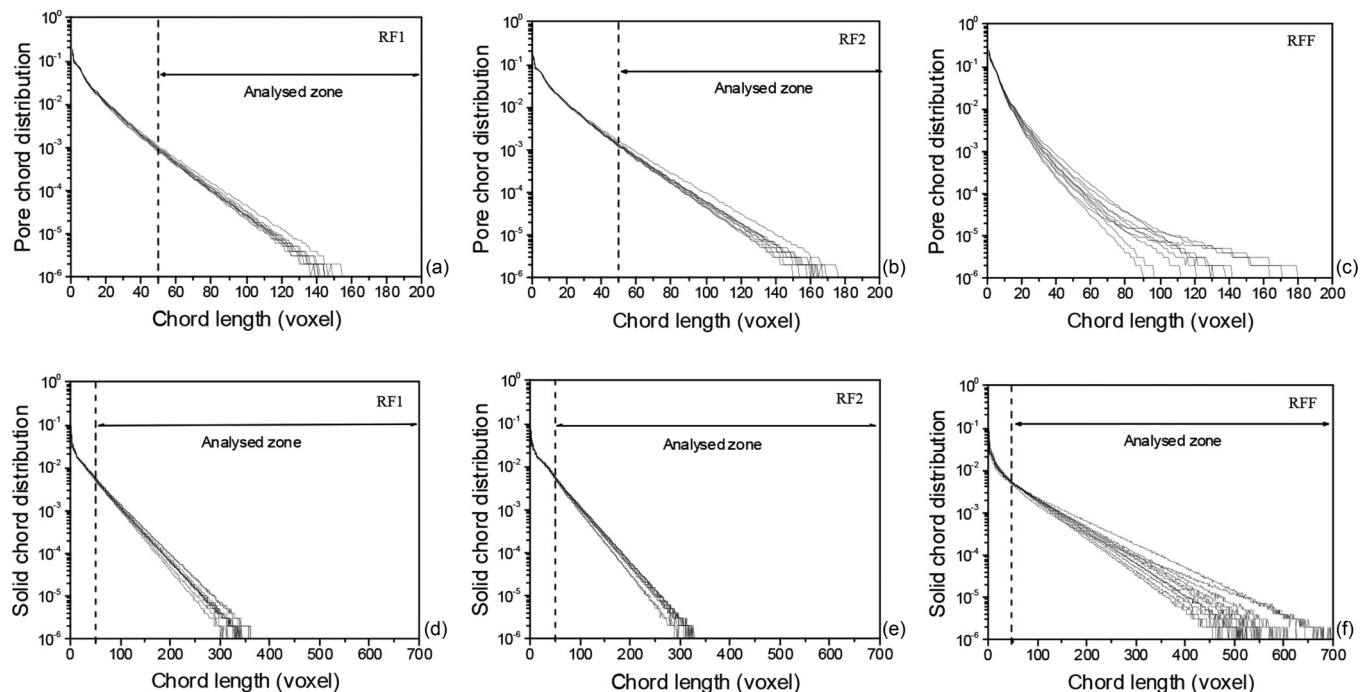


FIG. 7. Chord length distribution for the 30 samples (top: pore phase, bottom: solid phase): (a) and (d) for the RF1 samples, (b) and (e) for the RF2 samples, (c) and (f) for the RFF samples.



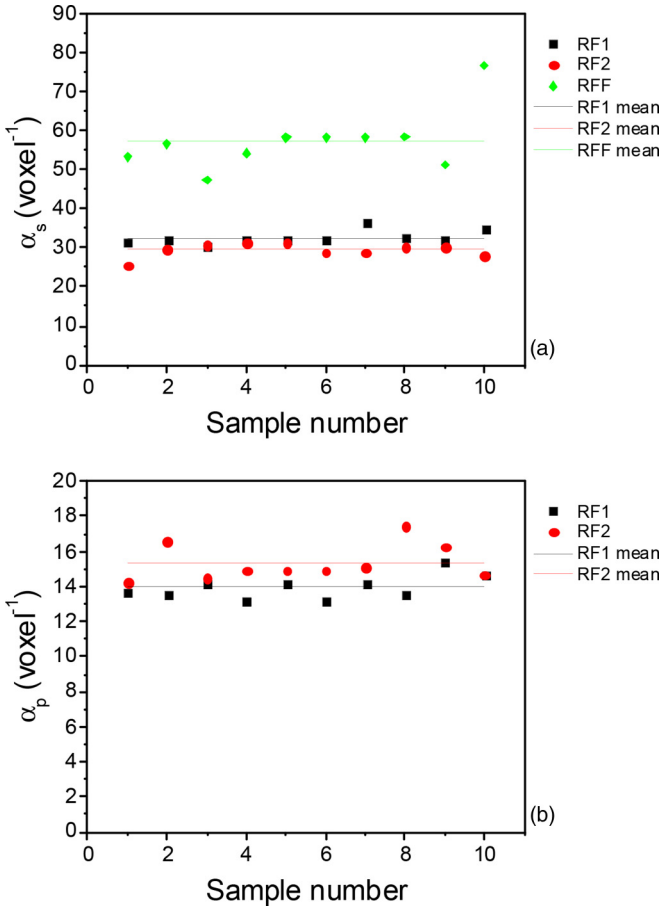


FIG. 8. (Color online) Characterization of the persistence length for the 30 analyzed samples. The persistence lengths were calculated on the whole sample volumes ( $1300 \times 1300 \times 1000$  voxels). The continuous lines are the mean values of the ten values recorded for each sort of stone.

enable the different types of stones to be distinguished using the correlation length  $l_c$ . The  $L$  values distinguish between RFF and RF1/RF2 stone types but, due to the strong data variance, it is difficult to discriminate between the RF1 and RF2 samples.

### 3. Chord length

The pore and solid chord distributions were measured for the 30 samples (Fig. 7). The pore and solid chord distributions for the ten RF1 and the ten RF2 samples decreased exponentially. These stones were therefore classified as long-range random media. The solid chord distributions of the ten RFF samples also decreased exponentially, while their pore chord distributions showed more complex morphologies (Fig. 7). This is probably due to the occasional presence of large fossils

that can create large pores. Furthermore, the dispersion of the chord distributions in the RFF samples is higher than in the other samples.

As all the chord distributions (except for the pore chord distribution of the RFF samples) decrease exponentially, they were fitted by Eqs. (2) and (3) in the long chord range (i.e.,  $r > 50$  voxels) and the persistence lengths are reported in Fig. 8 and in Table I. For the RF1 and RF2 samples, the mean persistence lengths for the porous phase and the solid phase were close but distinct (Fig. 8). Furthermore, the two sets of pore chord distributions (and solid chord distributions) are not superimposed. The dispersions observed for these two sets of stones illustrate the slight differences (of grain size, for example) and/or the heterogeneities in the media for the studied volumes, at the image resolution used. These two stones can therefore be considered similar, and even if the differences between them are weak, they are distinguishable. The RFF chord distributions (pore and solid) are clearly distinct from the RF1 and RF2 chord distributions. This is confirmed by the mean persistence length of the RFF samples for the solid phase, which is about 66% (about 84%, respectively) higher than the mean persistence length of the RF1 samples (RF2 samples, respectively). Hence, the porous media of the RFF samples are clearly different from those of the other two stones, and the strong dispersions show that the RFF samples are more heterogeneous than the others. To conclude, the chord distributions enable the distinction not only between the RFF and RF1/RF2 stone types, but also between the RF1 and RF2 samples.

## C. Representativity

Two types of analysis were carried out to evaluate the representativity of a sample or a set of samples. In the following, the side length  $l$  represents the cubic root of the volume.

### 1. Porosity

The representativity of each sample from each stone type was tested using the approaches of Gusev [20] and Kanit [18]. The porosity was measured for five independent subvolumes of different side lengths on the 30 samples. Results are presented in Figs. 9(a)–9(c) for one sample of each sort of stone. The scatter, as defined by Gusev [20], appears to be small enough (less than 0.015) for a side length larger than  $l = 200$  voxels. To refine these results, the method proposed by Kanit [18] was applied to estimate a representative volume for a given error and a number of realizations. We chose a single realization ( $n = 1$ ) and an error of 5%. The results for the 30 samples are presented in Table II. It can be seen that, for each sample, the volume obtained for the REV is smaller than the field of view. This means that the sample is locally homogeneous. However, depending on the type of stone, the volume obtained

TABLE I. Mean structural characteristics (porosity, autocorrelation function, and chord distribution).

Sample	Porosity [–]	$l_c$ [voxels]	$L$ [voxels]	$\alpha_p$ [voxels $^{-1}$ ]	$\alpha_s$ [voxels $^{-1}$ ]
RF1	$0.237 \pm 0.010$	$591.5 \pm 19.5$	$18.83 \pm 1.15$	$13.97 \pm 0.66$	$32.68 \pm 1.66$
RF2	$0.274 \pm 0.010$	$583.5 \pm 35.4$	$18.88 \pm 0.57$	$15.35 \pm 1.00$	$29.51 \pm 1.68$
RFF	$0.101 \pm 0.016$	$590.5 \pm 14.3$	$24.18 \pm 1.20$	–	$57.31 \pm 7.35$

can vary. For RF1 samples  $l_{REV}$  varies from a minimum value  $l_{REV}(\min) = 194$  voxels to a maximum value  $l_{REV}(\max) = 388$  voxels. This also holds for the other two stones:  $l_{REV}(\min) = 185$  voxels and  $l_{REV}(\max) = 522$  voxels for RF2 stone;  $l_{REV}(\min) = 281$  voxels and  $l_{REV}(\max) = 692$  voxels for RFF stone.

**2. Chord length distribution**

A similar approach was adopted for a single sample (the RF1 sample presented in Fig. 1) on chord distribution for the pore and solid phases. The results are shown in Figs. 9(d) and 9(e) for Gusev’s approach and in the text for Kanit’s approach. The scatter as defined by Gusev is smaller than 0.015 for cubic volumes whose side length is larger than 250 voxels. The methodology proposed by Kanit gives a  $l_{REV} = 250$  voxels for the persistence length in the solid phase and  $l_{REV} =$

125 voxels for the persistence length in the pore phase for a single realization and a relative error of 5%. The REV for chord length distributions is thus smaller than the imaged volume.

**3. Synthesis of the representativity analysis**

For all the samples, a REV for porosity exists and the volumes of the REV are always much smaller than the 3D image sizes. We were also able to find a REV to characterize chord distribution in the solid and pore phases. Therefore, all the functions and characteristics calculated within this study are valid and the observations made on the differences between the three types of stone are relevant.

The size of REV obtained for porosity is larger than that obtained for chord distribution. This is coherent with the fact that a REV depends on the property of interest [10,16,18,20].

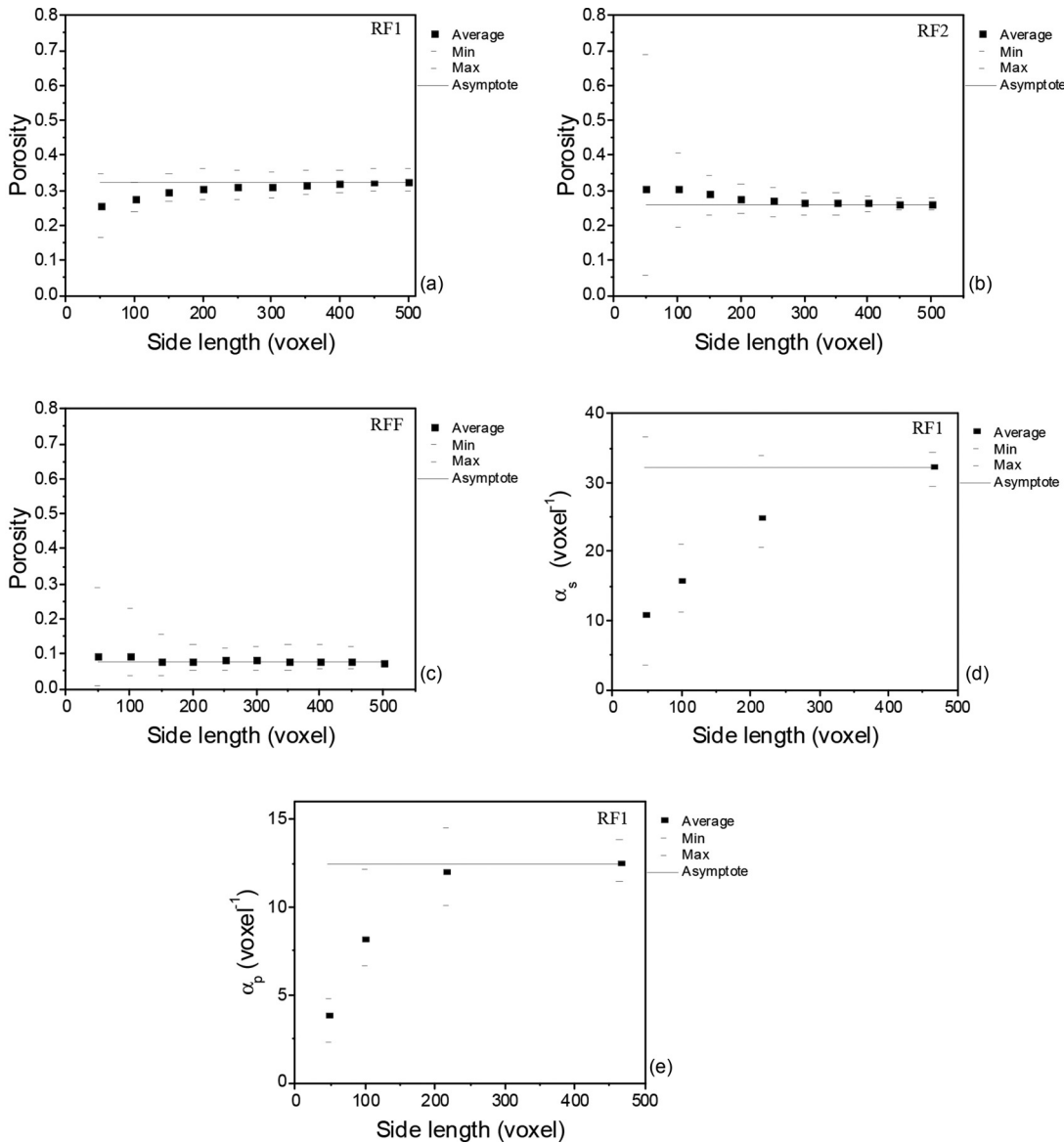


FIG. 9. Data evolved in the REV studies: porosity evolution as a function of the volume for five independent subvolumes for (a) an RF1 sample, (b) an RF2 sample, and (c) an RFF sample. Evolution of persistence lengths in the solid phase (d) and pore phase (e) for five independent subvolumes for the RF1 sample of Figs. 1 and 9(a). Black dots represent the minimum and maximum values. The continuous lines are the mean values of the five independent subvolumes.

TABLE II. Estimations of the representative elementary volumes (REV)s for porosity and corresponding cubic side lengths  $l_{\text{REV}}$  for an error of 5% and a single realization ( $n = 1$ ) for the 30 samples.

Sample	RF1		RF2		RFF	
	REV (voxels)	$l_{\text{REV}}$ (voxels)	REV (voxels)	$l_{\text{REV}}$ (voxels)	REV (voxels)	$l_{\text{REV}}$ (voxels)
1	$0.96 \times 10^9$	328.7	$0.98 \times 10^9$	331.0	$0.60 \times 10^9$	281.4
2	$1.12 \times 10^9$	346.2	$0.17 \times 10^9$	185.6	$3.17 \times 10^9$	489.8
3	$0.55 \times 10^9$	273.5	$0.71 \times 10^9$	297.0	$1.43 \times 10^9$	375.7
4	$1.58 \times 10^9$	388.3	$3.84 \times 10^9$	521.8	$3.12 \times 10^9$	487.0
5	$0.20 \times 10^9$	194.3	$0.52 \times 10^9$	269.0	$8.95 \times 10^9$	692.1
6	$0.85 \times 10^9$	315.9	$1.23 \times 10^9$	357.6	$1.52 \times 10^9$	383.5
7	$0.86 \times 10^9$	316.9	$0.43 \times 10^9$	251.2	$6.25 \times 10^9$	614.1
8	$1.31 \times 10^9$	365.2	$2.04 \times 10^9$	422.5	$1.38 \times 10^9$	371.0
9	$0.57 \times 10^9$	277.4	$0.25 \times 10^9$	210.6	$1.86 \times 10^9$	409.8
10	$1.13 \times 10^9$	347.3	$1.60 \times 10^9$	390.0	$1.31 \times 10^9$	364.3
Average	$0.91 \times 10^9$	315.4	$1.18 \times 10^9$	323.6	$3.06 \times 10^9$	446.9
Standard deviation	$0.38 \times 10^9$	52.7	$1.05 \times 10^9$	97.7	$2.76 \times 10^9$	119.1

As the REV volume depends on the location of the sample within the block of stone, i.e., it depends on the local heterogeneities within the stone, it would be more accurate to speak of locally homogeneous media.

It appears that the side lengths for porosity  $l_{\text{REV}}$  have the same order of magnitude as the correlation length  $l_c$  or are close to 10 times the solid persistence lengths  $\alpha_s$ . The side length of the REV estimated from the chord size distributions has the same order of magnitude of  $10 \times L$ . This may indicate that the correlation function and the lengths that characterize it suffice to decide whether a volume is representative or not for porosity or chord size distribution. One limitation of this analysis is that the chord size distributions must be fitted by functions that are representative of the structural disorder of porous media [31]. This was not possible in the present study, for example, for the pore chord distributions of the RFF samples. The calculation or simulation can therefore be done on a smaller volume than the imaged one, which saves computing time.

Finally, thanks to these criteria, all the microstructural measurements presented in a previous study conducted on the whole imaged volume [33] are validated.

#### IV. CONCLUSIONS

We have presented in this article a complete methodology to analyze the microstructural properties of complex porous media such as stones from 3D microtomography images. We focused particularly on the segmentation step, as this determines the final results. In the present study, a simple 3D mean filter sufficed to denoise the 3D images and hence easily separate the solid phase from the porous phase. In some cases, this preprocessing step is not so easy and a more sophisticated strategy must be employed (e.g., [37]).

A statistical study was carried out on 30 samples for three sorts of stones (ten for each sort of stone) showing that statistical representative elementary volumes (REV)s exist for these media and are reached for image sizes of  $1300 \times 1300 \times 1000$  voxels. Fortunately, we have also shown that it is not necessary to carry out an extensive study on ten samples (or more!) each time for each new porous medium, as general criteria have been established: the length for porosity  $l_{\text{REV}}$  is on the same order of magnitude as the correlation length  $l_c$ , and the side length of the REV for the chord size distribution has the same order of magnitude of  $10 \times L$ . In other words, it is sufficient to (i) acquire the largest 3D image possible at a given resolution, (ii) calculate the autocorrelation function, and (iii) use at least one of these two criteria to check whether the REV is reached. On that condition, the different characteristics observed on the 3D images are relevant and validated. This is the case for the three types of stone studied here.

The estimators used enabled two sorts of porous media to be quantitatively distinguished, namely, the two RF stones from the RFF stone. They are also sufficiently sensitive to observe local inhomogeneities in the media and hence, to separate two similar media (RF1/RF2) that present subtle differences. This means that the quantitative study of material modifications such as dissolution and recrystallization within a porous medium (e.g., weathering of stones, deformation of a structure, etc.) can be carried out, provided that the REV is imaged.

#### ACKNOWLEDGMENT

The authors gratefully acknowledge financial support provided by the Région Centre, France, under the PASTIS project.

- [1] N. Burlion, D. Bernard, and D. Chen, *Cem. Concr. Res.* **36**, 346 (2006).
- [2] A. Kaestner, E. Lehmann, and M. Stampanoni, *Adv. Water Resour.* **31**, 1174 (2008).
- [3] J. Lambert, I. Cantat, R. Delannay, A. Renault, F. Graner, J. A. Glazier, I. Veretennikov, and P. Cloetens, *Colloids Surf., A* **263**, 295 (2005).

- [4] M. Stampanoni, G. Borchert, P. Wyss, R. Abela, B. Patterson, S. Hunt, D. Vermeulen, and P. Rügsegger, *Nucl. Instrum. Methods Phys. Res., Sect. A* **491**, 291 (2002).
- [5] L. Salvo, P. Cloetens, E. Maire, S. Zabler, J. J. Blandin, J. Y. Buffière, W. Ludwig, E. Boller, D. Bellet, and C. Jossier, *Nucl. Instrum. Methods Phys. Res., Sect. B* **200**, 273 (2003).

- [6] J. Baruchel, J. Y. Buffiere, P. Cloetens, M. Di Michiel, E. Ferrie, W. Ludwig, E. Maire, and L. Salvo, *Scr. Mater.* **55**, 41 (1996).
- [7] W. J. Drugan and J. R. Willis, *J. Mech. Phys. Solids* **44**, 497 (1996).
- [8] R. Hill, *J. Mech. Phys. Solids* **11**, 357 (1963).
- [9] J. Bear, *Dynamics of Fluids in Porous Media* (Dover, New York, 1972).
- [10] R. Al-Raoush and A. Papadopoulos, *Powder Technol.* **200**, 69 (2010).
- [11] V. N. Ashihmin and I. A. Povyshev, *Math. Model Syst. Process* **3**, 11 (1995) [In Russian].
- [12] A. Borbely, H. Biermann, and O. Hartmann, *Mater. Sci. Eng., A* **313**, 34 (2001).
- [13] V. N. Bulsara, R. Talreja, and J. Qu, *Compos. Sci. Technol.* **59**, 673 (1999).
- [14] I. M. Gitman, H. Askes, L. J. Sluys, and M. Stroeven, *Multiscale Modelling of Granular Materials*, in *Proceedings of the Euro-C 2003, Computational Modelling of Concrete Structures*, edited by N. Bićanić, R. de Borst, H. Mang, and G. Meschke (Balkema, Rotterdam, 2003).
- [15] I. M. Gitman, M. B. Gitman, and H. Askes, *Arch. Appl. Mech.* **75**, 79 (2006).
- [16] S. Rolland du Roscoat, M. Decain, X. Thibault, C. Geindreau, and J.-F. Bloch, *Acta Mater.* **55**, 2841 (2007).
- [17] D. Zhang, R. Zhang, S. Chen, and W. E. Soll, *Geophys. Res. Lett.* **27**, 1195 (2000).
- [18] T. Kanit, S. Forest, I. Galliet, V. Mounoury, and D. Jeulin, *Int. J. Solids Struct.* **40**, 3647 (2003).
- [19] T. Kanit, F. N'Guyen, S. Forest, D. Jeulin, M. Reed, and S. Singleton, *Comput. Methods Appl. Mech. Eng.* **195**, 3960 (2006).
- [20] A. A. Gusev, *J. Mech. Phys. Solids* **45**, 1449 (1997).
- [21] O. Rozenbaum, L. Barbanson, F. Muller, and A. Bruand, *C. R. Geosciences* **340**, 345 (2008).
- [22] K. Beck, M. Al-Mukhtar, O. Rozenbaum, and M. Rautureau, *Building Environ.* **38**, 1151 (2003).
- [23] J. Baruchel, J. Y. Buffiere, E. Maire, P. Merle, and G. Peix, *X-Ray Tomography in Material Science* (Hermes Science, Paris, 2000).
- [24] E. Van de Casteele, D. Van Dyck, J. Sijbers, and E. Raman, *SPIE Medical Imaging: Image Processing*, Vol. 5370 (San Diego, CA, USA, 2004), pp. 2089–2096.
- [25] A. H. Lumpkin, B. X. Yang, C. Y. Yao, and L. Emery, *Proceedings of the 2003 Particle Accelerator Conference, Portland, Oregon*, Vol. 4 (IEEE, Piscataway, NJ, USA, 2003), pp. 2423–2425.
- [26] L. A. Feldkamp, L. C. Davis, and J. W. Kress, *J. Opt. Soc. Am. A* **1**, 612 (1984).
- [27] R. A. Ketcham and W. D. Carlson, *Comput. Geosci.* **27**, 381 (2001).
- [28] E. Le Trong, O. Rozenbaum, J. L. Rouet, and A. Bruand, *Image Anal. Stereol.* **27**, 175 (2008).
- [29] J. T. Bushberg, J. A. Seibert, E. M. Leidholdt, and J. M. Boone, *The Essential Physics of Medical Imaging* (Lippincott Williams & Wilkins, Philadelphia, 2006).
- [30] M. Coster and J. L. Cherman, *Précis d'Analyse d'Images* (Ed. du CNRS, Paris, 1985).
- [31] P. Levitz and D. Tchoubar, *J. Phys. I France* **2**, 771 (1992).
- [32] O. Rozenbaum, E. Le Trong, J. L. Rouet, and A. Bruand, *J. Cult. Heritage* **8**, 151 (2007).
- [33] O. Rozenbaum, *Sci. Total Environ.* **409**, 1959 (2011).
- [34] M. A. Ioannidis, M. J. Kwiecien, and I. Chatzis, *J. Pet. Sci. Eng.* **16**, 251 (1996).
- [35] D. A. Coker, S. Torquato, and J. H. Dunsmuir, *J. Geophys. Res.* **101**, 17497 (1996).
- [36] G. Matheron, *The Theory of Regionalized Variables and Its Applications* (School of Mines, Paris, 1971).
- [37] P. Iassonov, T. Gebrenegus, and M. Tuller, *Water Resour. Res.* **45**, W09415 (2009).